Energy Conversion and Management 149 (2017) 616–630

Contents lists available at ScienceDirect

Energy Conversion and Management

journal homepage: www.elsevier.com/locate/enconman

Effect of the shaft on the aerodynamic performance of urban vertical axis wind turbines

Abdolrahim Rezaeiha[a,*], Ivo Kalkman[b], Hamid Montazeri[a,b], Bert Blocken[a,b]

[a] Building Physics and Services, Department of the Built Environment, Eindhoven University of Technology, P.O. Box 513, 5600 MB Eindhoven, The Netherlands
[b] Building Physics Section, Department of Civil Engineering, KU Leuven, Kasteelpark Arenberg 40 – Bus 2447, 3001 Leuven, Belgium

ARTICLE INFO

Keywords:
Vertical axis wind turbine (VAWT)
Shaft (tower)
Performance improvement
CFD
URANS
Rotating rough cylinder

ABSTRACT

The central shaft is an inseparable part of a vertical axis wind turbine (VAWT). For small turbines such as those typically used in urban environments, the shaft could operate in the subcritical regime, resulting in large drag and considerable aerodynamic power loss. The current study aims to (i) quantify the turbine power loss due to the presence of the shaft for different shaft-to-turbine diameter ratios δ from 0 to 16%, (ii) investigate the impact of different operational and geometrical parameters on the quantified power loss and (iii) evaluate the impact of the addition of surface roughness on turbine performance improvement. Unsteady Reynolds-averaged Navier-Stokes (URANS) calculations are performed on a high-resolution computational grid. The evaluation is based on validation with wind-tunnel measurements. The results show that the power loss increases asymptotically with increasing δ due to the higher width and length of the shaft wake as the blades pass through a larger region with lower velocity in the downwind area. A maximum power loss of 5.5% compared to the hypothetical case without shaft is observed for $\delta = 16\%$. The addition of surface roughness is shown to be an effective approach to shift the flow over the shaft into the critical regime, reducing the shaft drag and wake width as a result of a delay in separation. For an optimal dimensionless equivalent sand-grain roughness height of 0.08, the turbine power coefficient at $\delta = 4\%$ improves by 1.7%, which is equivalent to a 69% recovery of the corresponding turbine power loss. The results are found to be virtually independent of the shaft-to-turbine rotational speed ratio.

1. Introduction

Vertical axis wind turbines (VAWTs) have regained interest during the last decade for application as large-scale multi-MW turbines in off-shore areas [1–3] and as small-scale turbines in urban environments [4,5]. The large-scale turbines are interesting for off-shore application due to their low manufacturing, installation and maintenance costs, scalability, robustness, reliability, and installation of the generator on the ground, while their omni-directional capabilities make them highly desirable for urban environments where the wind direction is frequently changing [6]. However, a significantly lower amount of research in the past three decades has resulted in VAWT performance falling behind that of their horizontal axis counterparts. Several research activities have recently focused on further understanding the complex unsteady aerodynamics of VAWTs [7–15] and characterizing their performance via parameters such as the number of blades [16], blade (airfoil) shape [17–20], turbine solidity [16,18,21] and blade pitch angle [22,23]. Employment of ducts [11], guide vanes [24–26] and utilization of flow control on turbine blades [27–31] also have recently received attention.

The tower is an inseparable component of horizontal and vertical axis wind turbines, which greatly affects the flow on the blades in its neighborhood. For an upwind horizontal axis wind turbine (HAWT) the effect is due to the blades passing through the stagnation region in front of the tower, while for a VAWT or a downwind HAWT this is due to the blades passing through the wake of the tower. A significant amount of research has been performed to characterize the effect of the tower shadow on the aerodynamic and structural performance of HAWTs [32–36]. In contrast, early research on VAWT focused on large turbines with a very small ratio of the tower diameter to turbine diameter. This results in a large relative distance between the tower (which can also be referred to as the shaft) and the blades, in which the effect of the shaft wake on the turbine aerodynamic performance was assumed to be negligible and was therefore not quantified in existing research [4]. However, this is not the case for smaller urban-scale VAWTs with comparatively large shaft-to-turbine diameter ratios, as the turbine power loss due to the blades passing through the wake of the shaft could be substantial. However, to the best of our knowledge, a detailed

* Corresponding author.
E-mail address: a.rezaeiha@tue.nl (A. Rezaeiha).

http://dx.doi.org/10.1016/j.enconman.2017.07.055
Received 13 June 2017; Received in revised form 25 July 2017; Accepted 26 July 2017

Nomenclature

A	turbine swept area, $h{\cdot}d$ [m^2]
c	blade chord length [m]
C_d	sectional drag coefficient [–]
C_f	skin friction coefficient [–]
C_l	sectional lift coefficient [–]
C_m	instantaneous moment coefficient [–]
C_P	power coefficient, $P/(qAU_\infty)$ [–]
C_T	thrust coefficient, $T/(qA)$ [–]
CoP	pressure coefficient [–]
d	turbine diameter [m]
D	cylinder diameter [m]
d_s	turbine shaft diameter [m]
f	frequency of vortex shedding [Hz]
F_s	safety factor [–]
h	turbine height [m]
k	turbulence kinetic energy [m^2/s^2]
k_s	equivalent sand-grain roughness height [m]
M	turbine moment [Nm]
n	number of blades [–]
P	turbine power [W]
q	dynamic pressure [Pa]
R	turbine radius [m]
Re_c	airfoil chord-based Reynolds number [–]
Re_{crit}	critical Reynolds number [–]
Re_D	cylinder diameter-based Reynolds number, DU_∞/ν [–]
Re_s	turbine shaft diameter-based Reynolds number, $d_s U_\infty/\nu$ [–]
Re_θ	momentum-thickness Reynolds number [–]
St	Strouhal number
t	time [s]
T	turbine thrust force [N]
TI	turbulence intensity [%]
U_∞	freestream velocity [m/s]
δ	shaft-to-turbine diameter ratio [–]
γ	intermittency [–]
η	shaft-to-turbine rotational speed ratio [–]
θ	azimuth angle [°]
λ	tip speed ratio [–]
ν	kinematic viscosity of air [m^2/s]
σ	solidity [–]
φ	circumferential angle on the cylinder (shaft) [°]
ω	specific dissipation rate [1/s]
Ω	turbine rotational speed [rad/s]
Ω_s	shaft rotational speed [rad/s]

study on the effect of the shaft on the aerodynamic power loss of urban-scale VAWTs has not yet been performed. Moreover, due to strong Reynolds number effects on flow over cylinders [37], the down-scaling of the turbine shaft in urban-scale VAWTs would most probably result in the shaft operating in the subcritical regime. Note that for a smooth cylinder the critical diameter-based Reynolds number corresponds to $Re_s < 2.5 \times 10^5$ [38]. This leads to a relatively large drag and massive flow separation [39], which can subsequently magnify the corresponding turbine power loss. This further emphasizes the importance of such a study.

The extensive literature on the loading and flow field of cylinders, either smooth [38,39] or rough [40–43], stationary or rotating [44–47], can be very useful to identify the flow regime over the turbine shaft and minimize the turbine power loss associated with the presence of its shaft. Previous studies have shown [39–41] that adding roughness to the surface can promote the laminar-to-turbulent transition in the boundary layer, consequently delaying flow separation over the cylinder and eventually significantly decreasing the cylinder drag coefficient C_d by shifting the flow to the critical regime. A reduction in drag, a delay in flow separation and a consequent reduction in wake width together with a jump in the shaft Strouhal number St can signal this shift in flow regime [40,41]. The thinner shaft wake can, in turn, result in turbine blades passing through a region containing more energy on the downwind side that could potentially lead to less power loss due to the presence of the shaft.

The current study is performed in three steps:

(1) The turbine power loss associated with the turbine shaft for different shaft-to-turbine diameter ratios δ from 2% to 16%, relevant for small- to medium-scale VAWTs, is quantified. The results are then compared with those for a hypothetical turbine with no shaft.
(2) The impact of different operating conditions (including inlet turbulence intensity, chord-based Reynolds number and tip speed ratio) and geometrical characteristics (including solidity and number of blades) on the quantified power loss is investigated.
(3) The flow regime over the turbine shaft is identified. Then the effect of the shaft surface roughness is investigated in order to find the optimal roughness height corresponding to the critical Reynolds number Re_{crit}, where a minimum shaft drag is achieved. The corresponding effect on the turbine aerodynamic performance is then investigated in detail. The dependence of the performance of the turbine with optimal roughness height on the shaft-to-turbine rotational speed ratio η is then studied in the range from 0 to 1, where 0 corresponds to a stationary shaft and 1 to a shaft rotating at the same rotational speed and direction as the turbine.

Unsteady Reynolds-averaged Navier-Stokes (URANS) simulations are performed on a high-resolution computational grid. The evaluation is based on validation with wind-tunnel measurements of flow over smooth and rough cylinders by [40,41,48], and for a VAWT by [49,50].

The outline of the paper is as follows: Section 2 presents a description of the computational settings and parameters where the geometrical and operational characteristics, computational domain, grid and other numerical settings and validation studies for both (smooth and rough) cylinders and the turbine are presented. The results of the study on the quantification of the turbine power loss due to the presence of the shaft for different shaft-to-turbine diameter ratios δ are discussed in Section 3.1. Section 3.2 presents a sensitivity analysis to investigate the effect of different operational and geometrical parameters on the turbine power loss due to the presence of the shaft. The possibility of turbine power improvement by addition of surface roughness to the shaft is discussed in Section 4.1. Section 4.2 explains the effect of the shaft-to-turbine rotational speed ratio η on the findings. The limitations of the work, recommendations for future work and the conclusions are provided in Section 5.

2. Computational settings and parameters

Given the main objectives of this study, it is important first to make sure that the flow around the shaft of the turbine, which is basically a cylinder (either smooth or rough), as well as the flow around the whole turbine is accurately simulated. Therefore, three sets of validation studies are performed where the geometrical and operational characteristics are selected to be the same or similar to those in the main study. The studied cases are (1) a stationary smooth cylinder at subcritical Re_D ($=DU_\infty/\nu$); (2) a stationary rough cylinder at subcritical and critical Re_D; and (3) a VAWT. CFD results of the VAWT have been extensively validated against experimental data of Tescione et al. [50] and the results, together with a comprehensive discussion of the possible explanations for observed deviations, have been published in [51].

A second validation study for a VAWT using similar computational settings has been performed and published in [23] where turbine C_P values at different tip speed ratios are compared against experimental data by Castelli et al. [49]. For brevity, these results and discussions are not repeated here. Instead, the simulations reported in Section 2.2.4 of this paper are solely intended to show that the turbulence model employed in the present study for the prediction of flow over the VAWT, namely the 3-equation *k-ω SST* model with intermittency transition submodel (*k-ω SST int.*), performs comparably to the already validated 4-equation *transition SST* model at the same operating conditions while reducing the calculation cost by solving one less equation. The geometrical and operational characteristics for each set of simulations are explained in this section.

2.1. Cylinder

2.1.1. Geometrical and operational characteristics

Two sets of validation studies are performed to provide confidence in the adapted approach for accurate simulation of the flow around both smooth and rough cylinders. The main geometrical and operational characteristics of the two studies are described in Table 1. As it will be discussed in Section 3, the smooth shaft of an urban-scale VAWT operates in the subcritical regime. Therefore, the validation study on a smooth cylinder also focuses on this regime. Note that the addition of surface roughness to the shaft can shift the flow over the turbine shaft from the subcritical to the critical regime. In the validation study for the rough cylinder, therefore, different roughness heights with Re_D corresponding to the subcritical and critical regimes are employed. As Re_{crit} decreases with increasing roughness height (see Eq. (1) [52,53]), lower Re_D is selected for the highest roughness height to keep the flow regime critical. The critical regime is chosen to maximize the similarity between the validation study on the rough cylinder and the flow regime over the rough turbine shaft, which is subcritical to critical.

$$Re_{crit} = \frac{6000}{\sqrt{k_s/D}} \quad (1)$$

2.1.2. Computational domain and grid

The two-dimensional computational domain employed for the simulation of flow around the cylinder (Fig.1a) has the origin at the cylinder center. The distance from the cylinder center to the domain inlet and outlet is 10*D* and 15*D*, respectively, and the domain width is 20*D*. A fully structured grid (Fig. 1b and c) is generated where the maximum y^+ over the cylinder is less than 4 and the total number of cells is approximately 120,000. The boundary layer grid over the cylinder is shown in Fig.1d.

2.1.3. Other numerical settings

In the simulations, the mean velocity and turbulent intensity inlet boundary conditions are uniform profiles according to the measured data. The approach-flow total turbulence intensity at the domain inlet is 0.6% and 0.7% for the smooth and rough cylinders while the incident total turbulence intensity is 0.57% and 0.67%, respectively [51,54,55]. Zero static gauge pressure is applied at the outlet plane. A symmetry condition on the sides and a no-slip condition on the cylinder wall is employed.

URANS calculations are performed with second-order spatial and temporal discretization and *SIMPLE* pressure-velocity coupling using the commercial flow solver ANSYS/Fluent 16.1 [56]. The calculations are initialized with steady-state RANS. The time step for the unsteady calculations is 0.001 s with 20 iterations per time step. Data sampling is initiated after 6000 time steps (6 s), which is equal to more than 10 flow-through times. The initialization time is found to be sufficient for the cylinder drag coefficient to reach a statistically steady state for all the tested cases. The sampled data are then averaged over 4000 time steps (4 s). Note that the averaging period is selected to correspond to more than 15 vortex shedding cycles for all the cases [57]. The modeling of turbulence is done using a 3-equation turbulence model, i.e. *k-ω SST* with the intermittency transition model (*k-ω SST int.*) [58]. This model solves an additional equation for intermittency γ over those of the popular 2-equation *k-ω SST* turbulence model to provide a better prediction of the laminar-to-turbulent transition. Intermittency-based turbulence models have been shown to perform well for wall-bounded flows where the development of the boundary layer and the laminar-to-turbulent transition play an important role in the overall flow characteristics, e.g. flow over airfoils and cylinders [59,60].

In ANSYS/Fluent, for *ω*-based turbulence models, the surface roughness is modeled using the modified law-of-the-wall for roughness developed by Cebeci and Bradshaw [61] based on Nikuradse's data on flow in sand-grain roughened pipes [62]. For these turbulence models, a singularity in the modified law-of-the-wall can occur for large roughness heights at low values of y^+. In order to avoid this issue, the wall is virtually shifted by half of the height of the roughness elements, following the work by Schlichting [63], which proposes that for tightly-packed uniform sand-grain roughness the blockage effect induced in the boundary layer is equivalent to 50% of the height of the roughness elements. Therefore, this virtual shift in the wall distance by half the roughness height results in a corrected value of y^+ for the first cell adjacent to the wall, thus avoiding the singularity. A roughness constant C_s of 0.5 is employed, representing a tightly-packed uniform sand-grain roughness [56]. Further details on the modeling of roughness can be found in Schlichting [63].

2.1.4. Validation study: Comparison of CFD results and wind-tunnel experiments

The results of the present CFD simulations of flow over a smooth cylinder in the subcritical regime ($Re_D = 1.4 \times 10^5$) are compared against the experiment by Cantwell and Coles [48] and the URANS (with the k-ε RNG turbulence model) and LES calculations by Tutar and Holdø [64]. The results are provided in Table 2. The comparison shows a very good agreement between the present CFD results and the experimental data, within 3.3% for both drag coefficient and Strouhal number. As shown by Palkin et al. [57], the prediction of the laminar-to-turbulent transition is very important to predict the flow on cylinders accurately. The intermittency-based turbulence models can, therefore, be very suitable in this respect. The current study provides a better prediction of the drag coefficient than the LES study by Tutar and Holdø [64], whereas the LES study had a slightly lower deviation from the experiment for the Strouhal number. The former can be related to the high sensitivity of LES to grid quality, which might result in URANS outperforming LES on coarser grids [65–67].

Fig. 2 presents the profiles of the time-averaged normalized streamwise velocity along the symmetry line $y/D = 0$, in the wake of the smooth cylinder. A very good agreement between the present CFD study and the experiment in the prediction of the wake is observed. In this case, the average absolute deviation is about 0.04.

Results of the simulation of flow over a rough cylinder with different roughness heights ($1.1 \times 10^{-3} \leq k_s/D \leq 30.0 \times 10^{-3}$) in the subcritical and critical regime are compared against the experimental data of Achenbach [40] and Achenbach and Heinecke [41] in Table 3. A

Table 1
Geometrical and operational characteristics of the cylinder validation studies.

Parameter	Smooth [48]	Rough [40,41]
Cylinder diameter, D [m]	0.104	0.150
Cylinder dimensionless equivalent sand-grain roughness height, k_s/D	–	1.1×10^{-3}–30×10^{-3}
Inlet velocity, U_∞ [m/s]	20	2.85–7.80
Inlet turbulence intensity, TI [%]	0.6	0.7
Reynolds number, Re_D	140,000	29,000–80,000

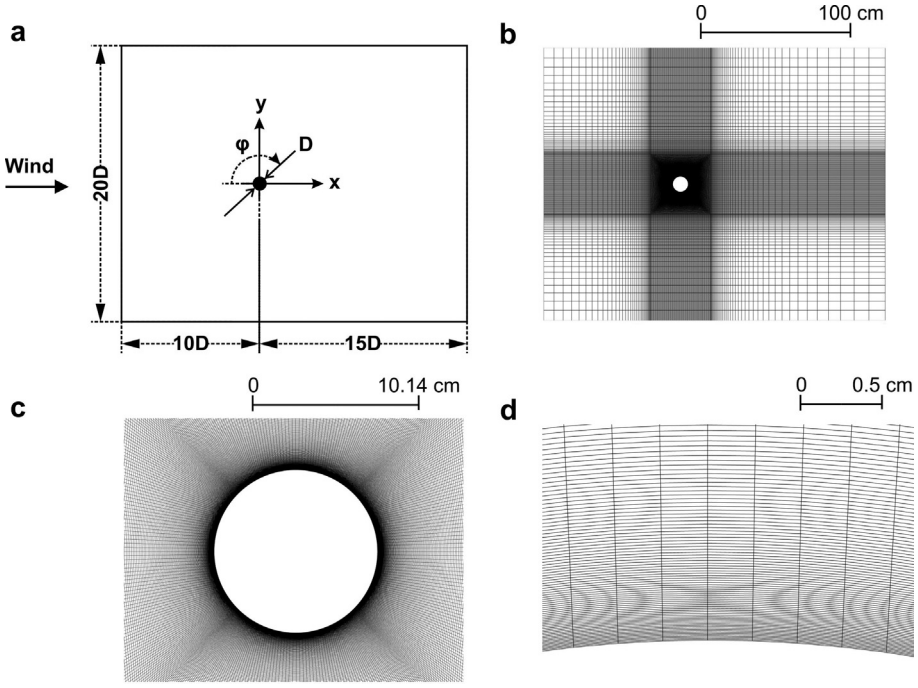

Fig. 1. (a) Schematic of the computational domain; computational grid (b) in the whole domain, (c) near the cylinder and (d) the boundary layer grid for simulation of flow over a smooth cylinder. A similar domain and grid are used for the rough cylinder.

good agreement is observed for both drag coefficient and Strouhal number, with a maximum deviation of 9.4% for the drag coefficient and 8.3% for the Strouhal number. Moreover, the trend of drag coefficient as a function of k_s/D is quite well produced. In this case, the drag coefficient reduces as k_s/D increases from 1.1×10^{-3} to 9.0×10^{-3}, and then increases with further increase in k_s/D (from 9.0×10^{-3} to 30.0×10^{-3}).

2.2. VAWT

2.2.1. Geometrical and operational characteristics

Flow around a two-bladed H-type VAWT with a solidity of 0.12, a diameter of 1 m, a height of 1 m and a swept area of 1 m^2 is simulated. The turbine blade section is a *NACA0018* airfoil with a chord of 0.06 m. The turbine has a smooth shaft with a diameter of 0.04 m, which is rotating in the same direction as the turbine with the same rotational speed, resulting in a shaft-to-turbine diameter ratio δ of 4% and a shaft-to-turbine rotational speed η of 1, where δ and η are given by Eqs. (2) and (3), respectively. The turbine operates at a moderate tip speed ratio of 4.5. The freestream velocity is 9.3 m/s with 5% turbulence intensity, and the turbine rotational speed is 84 rad/s (800 rpm). The geometrical and operational characteristics of the turbine are described in Table 4 where the airfoil chord-based Reynolds number Re_c is defined using Eq. (4). It is important to note that Re_s is almost an order of magnitude lower than Re_c. In practice the experienced streamwise velocity upstream of the shaft is lower than the free stream velocity due to the energy extraction by blades passing on the turbine fore half ($0^\circ \leq \theta \leq 180^\circ$), leading to even lower Re_s values.

$$\delta = d_s/d \tag{2}$$

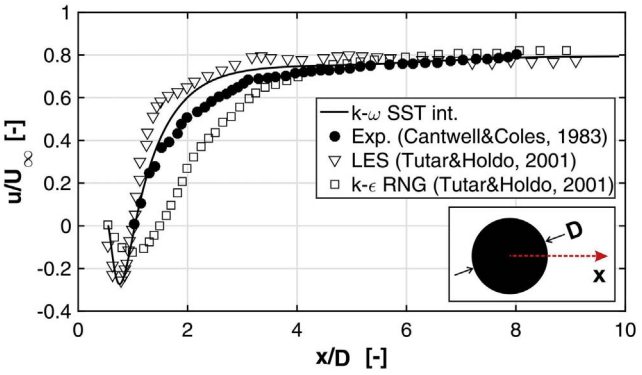

Fig. 2. Time-averaged normalized streamwise velocity along symmetry line $y/D = 0$ in the wake of a smooth cylinder in the subcritical regime ($Re_D = 1.4 \times 10^5$).

$$\eta = \Omega_s/\Omega \tag{3}$$

$$Re_c = (c\sqrt{(R\ \Omega)^2 + U_\infty^2})/\nu \tag{4}$$

2.2.2. Computational domain and grid

The simulations are performed in a two-dimensional domain. Note that an earlier study by Rezaeiha et al. [51] shows that using two- and three-dimensional domains leads to a negligible difference (< 1%) in the calculated turbine performance for the studied operating conditions. The main reason for this is that the low solidity and moderate tip speed ratio of the turbine minimize the complex 3D flow features associated with dynamic stall and blade-wake interactions. The computational domain consists of a rotating core (to facilitate the rotation of

Table 2
Comparison of present CFD results and experimental results [48] of drag coefficient and Strouhal number for a smooth cylinder in the subcritical regime ($Re_D = 1.4 \times 10^5$).

Parameter	*Exp.* [48]	*k-ω SST int.*		*LES* [64]		*k-ε RNG* [64]	
	Value	Value	Deviation from Exp. (%)	Value	Deviation from Exp. (%)	Value	Deviation from Exp. (%)
C_d	1.23	1.19	−3.2	1.40	13.8	0.98	−20.3
St	0.179	0.185	3.3	0.184	2.8	0.167	−6.7

Table 3
Comparison of present CFD results and experimental results [40,41] of drag coefficient and Strouhal number for a rough cylinder in the subcritical and critical regime.

k_s/D	Re_D	Re_{crit}	Parameter	Exp.	k-ω SST int.	
				Value	Value	Deviation from Exp.
1.1×10^{-3}	79,000	200,000	C_d	1.04	0.99	−4.8%
			St	–	0.201	–
4.5×10^{-3}	80,000	90,000	C_d	0.85	0.93	9.4%
			St	–	0.212	–
9.0×10^{-3}	76,000	65,000	C_d	0.80	0.84	5%
			St	0.24	0.22	−8.3%
30.0×10^{-3}	29,000	30,000	C_d	1.06	1.01	−4.7%
			St	0.243	0.246	1.2%

Table 4
Geometrical and operational characteristics of the VAWT.

Parameter	Value
Number of blades, n	*2*
Diameter, d [m]	1
Height, h [m]	1
Swept area, A [m^2]	1
Tip speed ratio, $\lambda = \Omega R/U_\infty$ [–]	4.5
Solidity, $\sigma = nc/d$ [–]	0.12
Airfoil	NACA0018
Airfoil chord, c [m]	0.06
Shaft diameter, d_s [m]	0.04
Freestream velocity, U_∞ [m/s]	9.3
Turbine rotational speed, Ω [rad/s]	83.8
Shaft rotational speed, Ω_s [rad/s]	83.8
Airfoil chord-based Re, Re_c	177,000
Shaft diameter-based Re, Re_s	26,000

the turbine), which is connected to the surrounding fixed domain using a non-conformal interface with sliding grid (Fig. 3). The distances from the turbine center to the domain inlet and outlet are 10*d* and 25*d*, respectively, with a domain width of 20*d* (blockage ratio 5%). The diameter of the rotating core is 1.5*d*. The domain size is selected according to the guidelines for VAWTs identified in an extensive systematic sensitivity study [51].

The computational grid consists of quadrilateral cells, as shown in Fig. 4, where a boundary layer grid with a maximum y^+ below 4 is employed on the walls. The two-dimensional grid has approximately 400,000 cells. The grid resolution resulted from a grid-convergence study using 3 grids generated based on an overall linear factor √2 for coarsening and refining [51]. The results of the gird-convergence study showed a negligible difference (< 1%) in the turbine power, and thrust coefficients (C_P and C_T) obtained on the three grids. The Grid Convergence Index (*GCI*) [68] was employed on C_P to quantify the discretization error for the coarse-medium grid pair using a safety factor (F_s) of 1.25, resulting in $GCI^{coarse} = 6.1 \times 10^{-3}$ (< 1.5% change in C_P) and $GCI^{fine} = 3.5 \times 10^{-3}$ (< 1% change in C_P). Therefore, the coarse grid is selected for the present study. Further details of the grid-convergence study can be found in Ref. [51].

2.2.3. Other numerical settings

The boundary conditions are a uniform constant velocity of 9.3 m/s at the inlet, zero static gauge pressure at the outlet, symmetry on the sides and a no-slip condition on the airfoil and shaft walls. The approach-flow uniform total turbulence intensity at the domain inlet is 5%, while the incident turbulence intensity is 4.42% [51,54,55].

URANS calculations are performed using the commercial CFD software package ANSYS/Fluent 16.1 [56]. Both spatial and temporal discretization is second-order, and pressure-velocity coupling is performed with the *SIMPLE* scheme. The solution from the steady RANS simulation is used for initialization after which 20 revolutions of the turbine are needed to reach a statistically steady state. Results are averaged over 10 revolutions where stated. The azimuthal increment ($d\theta$) utilized for the unsteady simulations is 0.1° with 20 iterations per time step to ensure all scaled residuals drop below 10^{-5}. The number of turbine revolutions in the initialization and data sampling phases and the employed azimuthal increment are selected according to the minimum requirements identified by Rezaeiha et al. [51,69]. Turbulence is modeled using two intermittency-based models: the 3-equation *k-ω SST* model with the intermittency transition submodel (*k-ω SST int.*) and, for the validation study only, the 4-equation *transition SST* turbulence model [58]. Both models are designed to provide a better prediction of the laminar-to-turbulent transition onset for wall-bounded flows as discussed in Section 2.1.3 [59]. The 4-equation turbulence model is already extensively validated [23,51] and the 3-equation model is shown (see Section 2.2.4) to have comparable performance with lower computational cost due to solving one less equation. The modeling of surface roughness for the turbine is the same as explained in Section 2.1.3 for the cylinder.

2.2.4. Validation study: Comparison of CFD results and wind-tunnel experiments

Table 5 presents the time-averaged (over 10 turbine revolutions) normalized streamwise and lateral velocity components at different downstream locations of the turbine ($2 \le x/R \le 4$; see Fig. 5). The results obtained by the 3-equation *k-ω SST* model with the intermittency transition submodel shows a lower average deviation from the experimental data than those by the *transition SST* model. The maximum average deviations for the streamwise velocity, which occurs at $x/R = 4$, are 12.6% and 16.4%, respectively. The turbine shaft C_d calculated using the 4-equation and 3-equation models in the two-dimensional simulations are 1.24 and 1.22, respectively. Zheng and Lei [60] showed that coupling of the intermittency transition model with the *k-ω SST* model improves the prediction of the flow pattern, separation point, drag coefficient and Strouhal number. This could be a possible explanation for the observed improvement. Despite this improvement, the current model does not provide any improvement in the prediction of the turbine wake asymmetry. A thorough discussion on the inability of the investigated models to predict this is given in Ref. [51].

3. Turbine power loss due to the presence of the shaft

3.1. Impact of shaft-to-diameter ratio

Simulations are performed for different shaft-to-diameter ratios (δ) to quantify the power loss due to the presence of the shaft. The turbine instantaneous moment coefficient (C_m) versus azimuth for the last turbine revolution for various δ from 2% to 16%, which are relevant ratios for urban-scale VAWTs, are compared in Fig. 6a. The results of the case without shaft is also shown in this figure. For the case with no

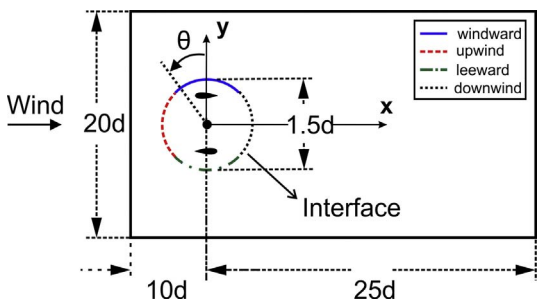

Fig. 3. Schematic of the computational domain (not to scale).

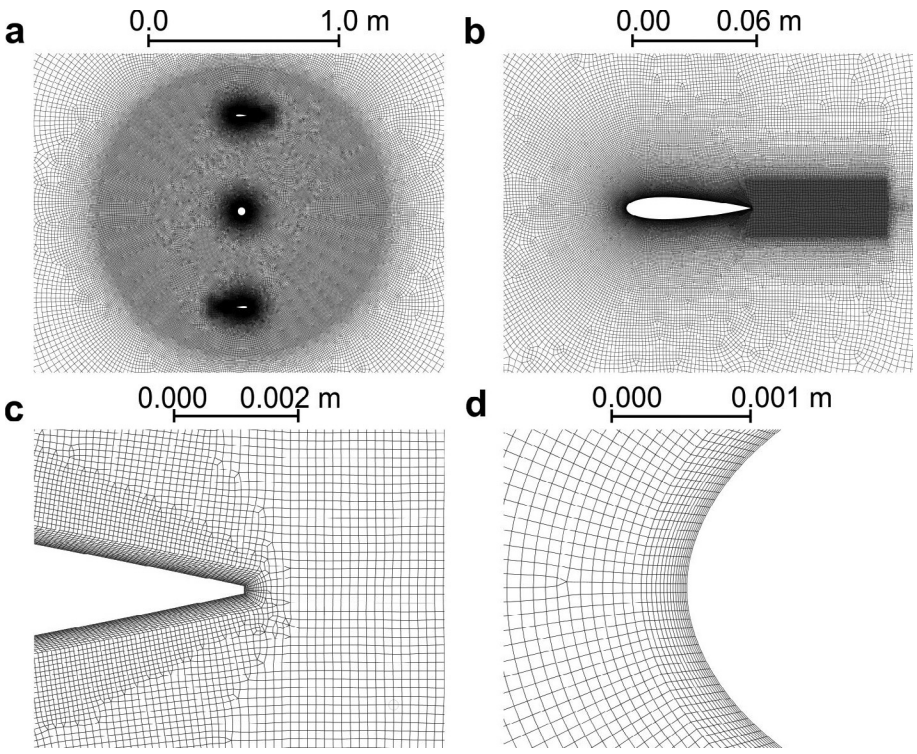

Fig. 4. Computational grid: (a) rotating core; (b) airfoil; (c) airfoil trailing edge; (d) airfoil leading edge.

Table 5
Average deviation of the time-averaged (over 10 turbine revolutions) normalized velocity from experiment [50].

	x/R	2.0	2.5	3.0	3.5	4.0
u/U_∞	*k-ω SST int.*	6.7	7.9	9.2	9.7	12.6
	transition SST	8.6	10.0	11.8	12.6	16.4
v/U_∞	*k-ω SST int.*	2.5	2.3	2.5	2.1	2.4
	transition SST	2.5	2.3	2.2	2.3	2.9

shaft, C_m stays almost constant on the downwind side of the revolution ($225^\circ \leq \theta < 315^\circ$). However, the presence of a shaft with $\delta \leq 4\%$ results in a drop in C_m near $\theta = 270^\circ$, as a result of the blade passing through the wake of the shaft. Note that strong interaction of the blade with the vortices shed by the shaft is hardly observed in the downwind quartile. In contrast, for $\delta > 4\%$, there is a clear effect of vortex shedding from the shaft on the C_m curve. In this case, a drop in C_m near $\theta = 270^\circ$ is observed while simultaneously an increase at neighboring values of θ is found. The change in turbine C_P for different values of δ is shown in Fig. 6b. The turbine power loss (regarding reduction in C_P) due to the presence of the shaft asymptotically increases from 0 to 5.5% with increasing δ from 0 (no shaft) to 16%.

The decrease in C_P with increasing δ can be associated with the increase in the width of the shaft wake at the downstream location where the blades pass ($x/d = 0.5$), as shown in Fig. 7. The increase in the width of the shaft wake occurs together with the decrease in the mean streamwise velocity. The time-averaged (over 10 turbine revolutions) normalized streamwise velocity at $x/d = 0.5$, averaged along the lateral line $-0.3 \leq y/d \leq 0.3$, decreases from 0.44 to 0.40 as δ increases from 2% to 12%. The asymptotic trend observed for C_P (see Fig. 6b) is because at high δ the complete blade trajectory on the downwind side intersects the shaft wake and the contribution of this quartile to the overall turbine performance, therefore, becomes negligible.

Fig. 8 presents contours of dimensionless out-of-plane vorticity ($\omega_z d_s/U_\infty$) in the wake of the shaft for different δ. It can be seen that the strength of the interactions between the blades and the shed vortices from the shaft increases non-linearly with increasing δ. As δ increases, the shaft wake interactions with the blade become stronger due to the larger size of the vortices passing through the blade trajectory, but also the smaller dimensionless streamwise distance (x/d_s) from the shaft to the blade trajectory. This is consistent with the trend observed for C_m in Fig.6a. Moreover, Fig. 8 indicates that separation on the leeward side ($y/d_s < 0$) of the rotating shaft happens later than on the windward side ($y/d_s > 0$) which is expected for a shaft rotating in counter-clockwise direction. This delay in separation on the leeward side is due to the fuller velocity profile in the boundary layer commonly observed for a downstream moving wall [70].

3.2. Sensitivity analysis: impact of operational and geometrical parameters

A sensitivity analysis is performed for other operational and geometrical conditions to further generalize the turbine power loss due to the presence of the shaft. The impact of several operational parameters including inlet turbulence intensity (TI), chord-based Reynolds number (Re_c) and tip speed ratio (λ), and geometrical parameters including solidity (σ) and number of blades (n) are investigated. Some of the main parameters of the cases that are investigated are given in Table 6.

The effort is made to investigate the effect of each parameter while the others are kept constant. Note that λ is normally changed by either altering Ω or U_∞. The former is employed in the current study, which means that while changing λ (for a given U_∞), Re_c is also altered. Similarly, solidity is typically modified by changing the blade chord length which means that (for a given U_∞ and Ω), Re_c also changes. The effect of number of blades is studied at constant blade chord length, which inevitably changes solidity as well.

Fig. 9a shows the impact of Re_c ($132 \times 10^3 \leq Re_c \leq 352 \times 10^3$) on the turbine power loss when the shaft is present ($\delta = 4\%$). This range corresponds to shaft diameter-based Reynolds number $29 \times 10^3 \leq Re_s \leq 76 \times 10^3$. Re_c is changed by increasing the free-stream velocity from 6.98 to 18.6 m/s while Ω is kept constant. The trend shows that by increasing Re_c from 132×10^3 to 352×10^3, the negative effect of the shaft on the turbine performance reduces as $|\Delta C_P|$ decreases from 2.5% to 1.6%. The aforementioned operating regime of

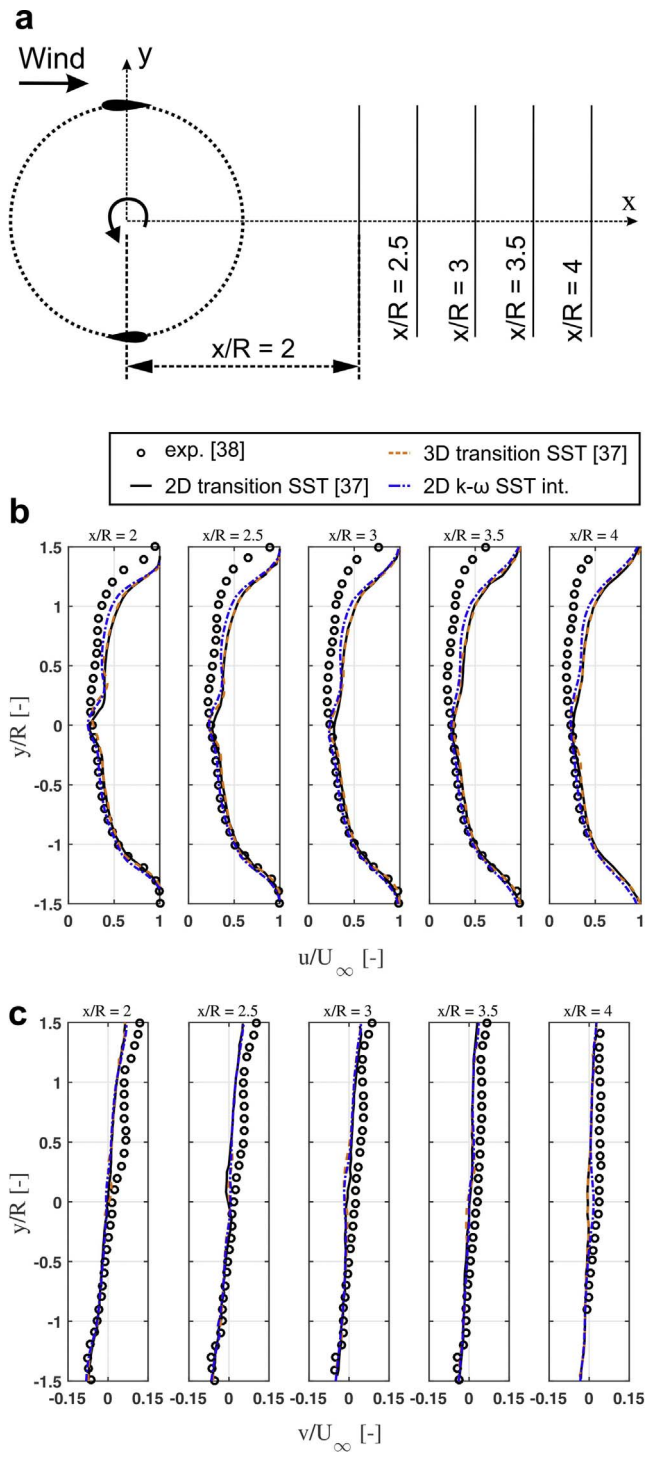

Fig. 5. (a) Downstream lateral sampling lines (not to scale); time-averaged (over 10 turbine revolutions) normalized (b) streamwise and (c) lateral velocities along lateral sampling lines compared against experiment [50].

the shaft corresponds to the subcritical regime for cylinders [39]. The studies on cylinders have shown [39,40] that within this regime increasing Re will shift the flow on cylinder towards critical, reduce the drag coefficient, delay the flow separation and abate the shaft wake width which eventually will enhance the turbine C_P. Further explanations on the effect of delay in separation on the shaft and the improvement in turbine aerodynamic performance are provided in Section 4.1.

The impact of inlet turbulence intensity on the turbine power loss

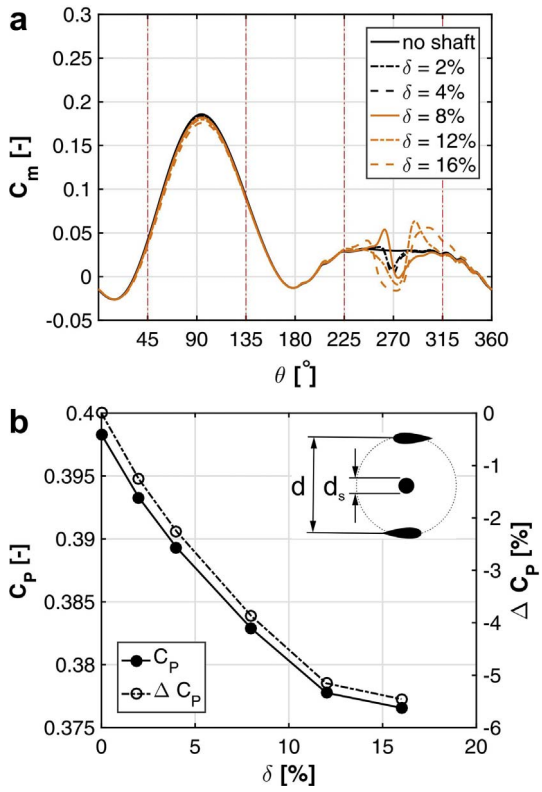

Fig. 6. (a) Instantaneous moment coefficient and (b) power coefficient and its relative change with respect to $\delta = 0$ for the last turbine revolution.

due to the shaft ΔC_P ($\delta = 4\%$) is shown in Fig. 9b. In this case, $0\% \leq TI \leq 10\%$, which corresponds to incident turbulence intensity [51,54,55] ranging from 0 to 7.9%. It can be seen that changing the inlet TI from 0 to 10% reduces $|\Delta C_P|$ from 2.6 to 1.9%. The increase in TI leads to the promotion of laminar-to-turbulent transition in the boundary layer on the shaft and consequently delays the separation and reduces the shaft wake, which benefits the turbine C_P (see Section 4.1 for further explanation).

Fig. 9c depicts the impact of tip speed ratio ($3.5 \leq \lambda \leq 5.5$) on the turbine power loss due to the shaft ΔC_P ($\delta = 4\%$). The tip speed ratio is altered by changing Ω at constant U_∞ which inevitably also changes Re_c between 139×10^3 and 214×10^3. Maximum turbine power loss due to the presence of the shaft occurs at the optimal tip speed ratio where the maximum C_P is generated. This shows that at the tip speed ratio where the turbine works most optimally the shaft creates the maximum loss of 2.3%. This value reduces to 1.8% and 1.2% at a tip speed ratio of 3.5 and 5.5, respectively. The smaller $|\Delta C_P|$ at $\lambda = 5.5$, compared to $\lambda = 3.5$, could be associated to higher Re_c at this λ.

The impact of solidity ($0.09 \leq \sigma \leq 0.18$) on the turbine power loss due to the shaft ΔC_P ($\delta = 4\%$) is illustrated in Fig. 9d. The solidity is modified by changing the blade chord length from 4.5 cm to 9 cm while keeping the number of blades constant. This results in Re_c varying from 132×10^3 to 264×10^3. The figure shows that increasing the solidity from 0.09 to 0.18 reduces $|\Delta C_P|$ from 2.5% to 1.9%. As the solidity increases, the relative size of the blade chord length to shaft diameter (and consequently shaft wake) increases. This results in the fact that when blades pass through the shaft wake, they are to a less extent affected by the shaft wake. Therefore, increasing the solidity and blade chord length reduce $|\Delta C_P|$.

Fig. 10 shows the impact of number of blades on the turbine power loss due to the shaft ΔC_P for a two- and three-bladed turbine with $\delta = 4\%$ and 8%. The blade chord length is kept constant. This makes the solidity change between 0.12 and 0.18. It can be seen that increasing the number of blades has a similar impact as increasing the

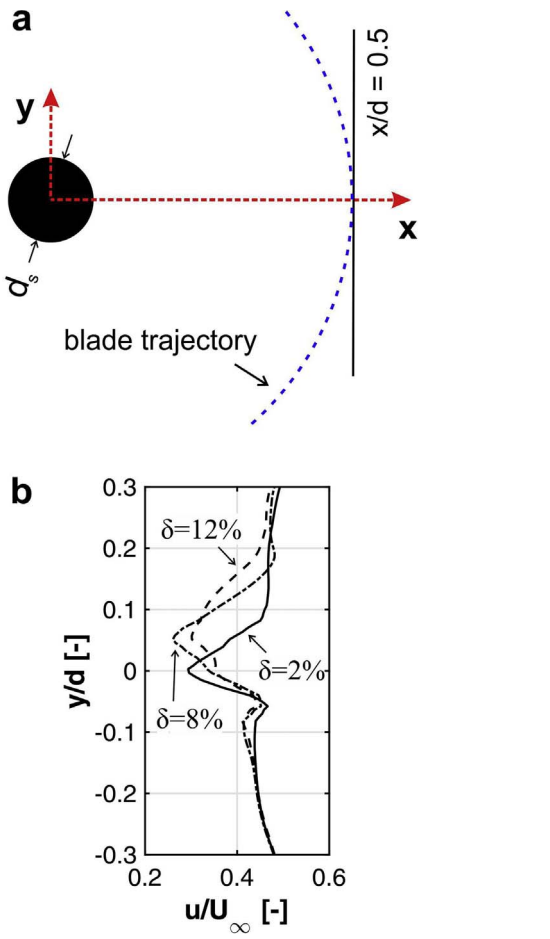

Fig. 7. (a) Downstream lateral sampling line in the wake of turbine shaft at $x/d = 0.5$ (not to scale); (b) time-averaged (over 10 turbine revolutions) normalized streamwise velocity along this line.

solidity (see Fig. 9d). $|\Delta C_P|$ reduces from 2.3% and 1.8% for $\delta = 4$ and from 3.9% to 1.2% for $\delta = 8$%., Increasing the number of blades results in more energy extraction in the fore half of the turbine, therefore, less energy can be potentially extracted in the aft half. This already results in less contribution of this region in the turbine total power production. As the power loss due to the shaft occurs in the aft half, less contribution of this region leads to a decrease in $|\Delta C_P|$. The reduction in $|\Delta C_P|$ by increasing number of blades becomes stronger when the power loss due to the shaft is also higher ($\delta = 8$%).

4. Turbine power improvement

4.1. Impact of shaft surface roughness

4.1.1. Average loading

The variations of C_P and C_T for the last turbine revolution with dimensionless equivalent surface roughness height k_s/d_s of the shaft are shown in Fig. 11a. It can be seen that adding roughness can increase C_P, with an optimal increase of 1.7% for $k_s/d_s = 0.08$. Since the power loss due to the presence of the turbine shaft ($\delta = 4$%) is 2.4% (Fig. 6b), no less than 69% of the power loss due to the presence of the shaft is regained. Higher k_s/d_s values will not further improve the performance of the turbine, as the flow on the cylinder most probably shifts to the supercritical regime [40]. A similar trend is observed for the thrust force (Fig. 11a), with an increase in C_T of 1.2%.

The time-averaged (over the last turbine revolution) drag and lift coefficients (C_d and C_l) of the shaft are shown in Fig. 11b. The optimum power coefficient (Fig. 11a) corresponds to the roughness height in

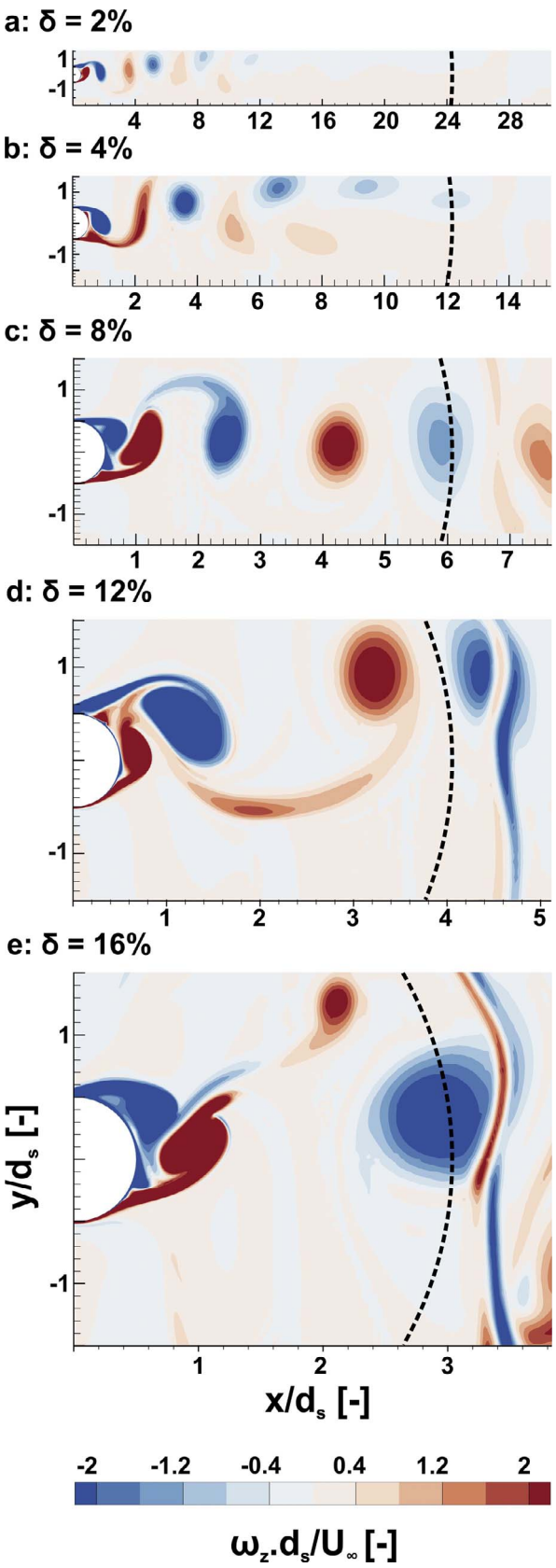

Fig. 8. Contours of instantaneous dimensionless out-of-plane vorticity in the wake of the shaft; the dashed line shows the blade trajectory.

Table 6
Some of the main parameters that are studied in the sensitivity analysis. Blade diameter is 1 m for all cases.

Parameter to study	n	δ [%]	σ	c [cm]	λ	U_∞ [m/s]	Ω [rad/s]	Re_c ($\times 10^3$)	TI [%]
Re_c	2	0, 4	0.12	6.0	4.5	6.98	62.77	132	5
						9.30	83.70	176	
						11.62	104.62	220	
						13.95	125.55	264	
						18.60	167.40	352	
TI	2	0, 4	0.12	6.0	4.5	9.30	83.70	176	0
									5
									10
									20
									30
λ	2	0, 4	0.12	6.0	3.5	9.30	65.10	139	5
					4.5		83.70	176	
					5.5		102.30	214	
σ	2	0, 4	0.09	4.5	4.5	9.30	83.70	132	5
			0.12	6.0				176	
			0.18	9.3				264	
n	2	0, 4, 8	0.12	6.0	4.5	9.30	83.70	176	5
	3		0.18						

Note: by changing λ and σ, Re_c is also altered. Also by changing n, σ is also changed.

which the minimum shaft $C_{d.}$ occurs. This implies that the power improvement of the turbine is partly a result of the reduced drag on the shaft itself. Furthermore, the variations of C_d as a function of k_s/d_s typically signals a shift from the subcritical to the critical regime for flow over cylinders [40]. In other words, increasing the roughness height will result in a reduction in the critical Reynolds number Re_{crit} and eventually, for an optimal roughness height, it will equal Re_s. An empirical correlation between k_s/d_s and Re_{crit} was deduced by Buresti [52] and Fage and Warsap [53] (see Eq. (1)). Based on this correlation, the identified optimal $k_s/d_s = 0.08$ yields $Re_{crit} \approx 21{,}000$, which is very close to the Re_s of the shaft provided in Table 4 ($Re_s = 26{,}000$). This further confirms that the observed reduction in shaft C_d and consequent turbine power recovery is due to the shift of the flow over the shaft from subcritical to critical.

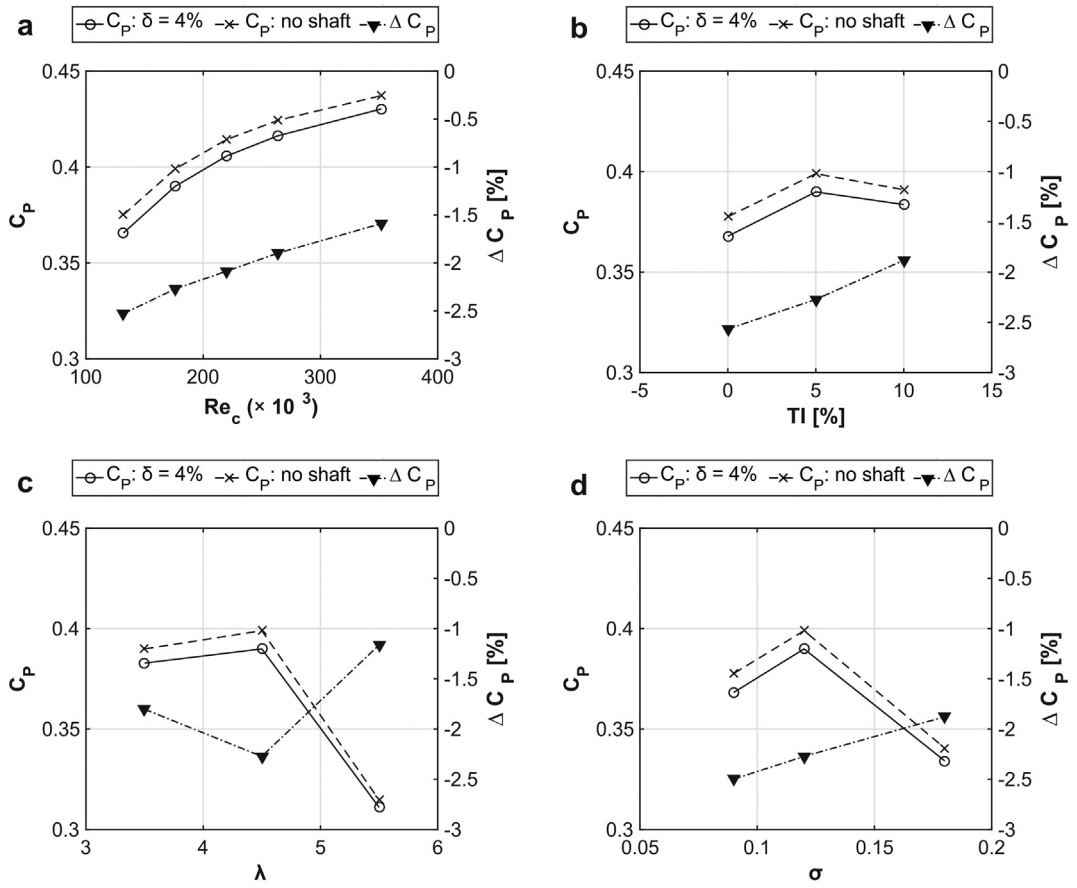

Fig. 9. The variations of turbine power loss due to the presence of the shaft for different (a) chord-based Reynolds number, (b) inlet turbulence intensity, (c) tip speed ratio and (d) solidity. $\delta = 4\%$ for all cases.

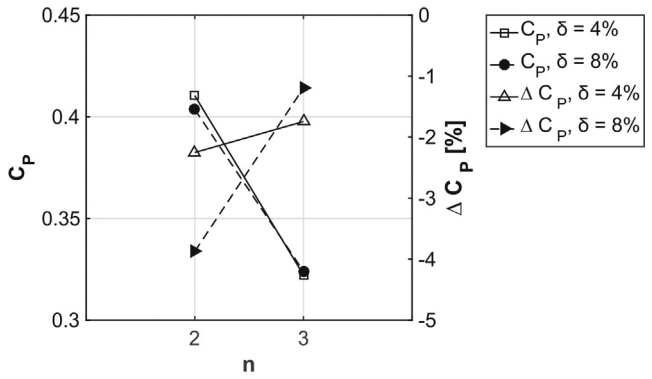

Fig. 10. The variations of turbine power loss due to the presence of the shaft for different number of blades.

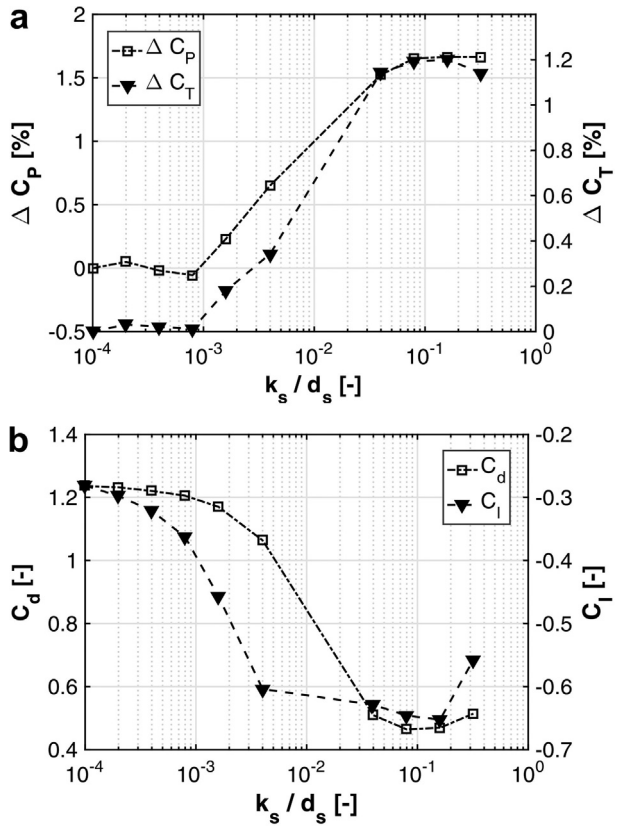

Fig. 11. Relative changes in four parameters concerning a smooth shaft for the last turbine revolution versus dimensionless equivalent sand-grain roughness height: (a) turbine coefficients of power C_P and thrust C_T; (b) time-averaged (over the last turbine revolution) drag (C_d) and lift (C_l) coefficients of the shaft.

4.1.2. Instantaneous loading

Fig. 12 compares the instantaneous moment coefficient for the last turbine revolution versus azimuth of the smooth and rough shaft with optimal $k_s/d_s = 0.08$. It can be observed that for the rough shaft, the power loss due to its presence is partially regained on the downwind side in the wake of the shaft (near $\theta \approx 270^{\circ}$), which results in the improvement of turbine C_P. The reason for this is discussed in Section 4.1.4.

To further elaborate on the effect of surface roughness on loads on the shaft, Fig. 13 compares the instantaneous drag and lift coefficients on the shaft for the last 10 turbine revolutions for the smooth and rough shaft. A significant reduction in the average value of C_d and the amplitudes of fluctuations of C_l and C_d is apparent for the rough shaft. Possible explanations will be discussed in Section 4.1.4.

4.1.3. Frequency analysis

The Strouhal number is calculated using Eq. (5), where f is the frequency of vortex shedding (corresponding to the highest peak in Fig. 14) and $U_{x,\exp}$ is the streamwise velocity experienced by the shaft, which is different from the freestream velocity due to the blades passing upstream of the shaft.

$$St = \frac{d_s f}{U_{x,\exp}} \tag{5}$$

The mean value of $U_{x,\exp} = 5.45$ m/s, calculated as the average over the lateral line $-2 \le y/d_s \le 2$ located upstream of the shaft at $x/d = -0.3$ ($x/d_s = -7.5$), is used for both smooth and rough shafts. Fig. 14 presents frequency analysis of the time series of lateral velocity over the last 10 turbine revolutions, corresponding to more than 20 shaft vortex shedding periods sampled in the wake of the shaft at $x/d_s = 1$ and $y/d_s = 0.5$. A jump in St from 0.19 to 0.23 between the smooth and rough shafts. This is in line with the results by Achenbach and Heinecke [41] in which a similar jump in St was observed for different roughness heights at Re_{crit} and typically signals a shift in the flow regime over the shaft from subcritical to critical.

4.1.4. Flow field

Vorticity contours with superimposed streamlines for the smooth and rough shaft are compared in Fig. 15. It can be seen that for the rough shaft the separation on both upper and lower surfaces of the shaft is delayed (see Table 7), although the delay is much more significant on the upper surface where the upstream-moving wall is more prone to separation. Here, the roughness in the boundary layer is shown to be more effective in increasing the resistance of the boundary layer to separation by adding extra momentum and promoting the laminar-to-turbulent transition. This also reduces the lateral asymmetry in the separation point locations on the upper and lower shaft surfaces as well as the shaft wake asymmetry.

In order to further elaborate on the delay in separation for the rough shaft, the profiles of time-averaged (over 10 turbine revolutions) normalized tangential velocity (V_φ/U_∞) on the upper surfaces of the smooth and rough shafts are compared at circumferential angles $70^{\circ} \le \varphi \le 125^{\circ}$, where separation is expected to happen in both cases (see Fig. 16). It is observed that the boundary layer is still attached for both shafts at $\varphi = 70^{\circ}$ while reverse flow ($V_\varphi/U_\infty < 0$) is already present for the smooth shaft at $\varphi = 80^{\circ}$. The separation grows for the smooth shaft with increasing φ while the flow stays attached up to $\varphi \approx 110^{\circ}$ for the rough shaft. At this point, reverse flow is also observed for the rough shaft, and the separation (regarding the radial distance of the location of zero velocity from the shaft wall) grows up to $\varphi = 125^{\circ}$. The observed delay in the separation over the rough shaft means that the amount of separated flow over the shaft has significantly decreased, which is the reason for the reduction in the amplitude of fluctuations of

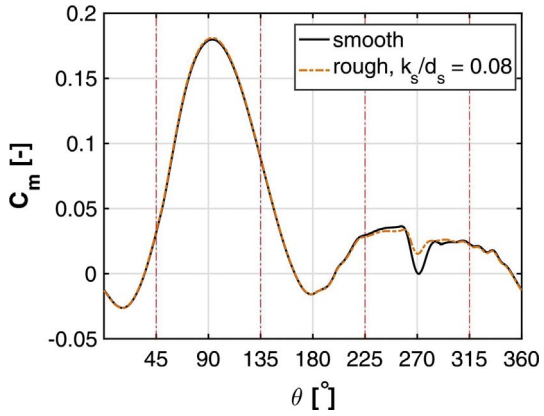

Fig. 12. Instantaneous moment coefficient for the last turbine revolution.

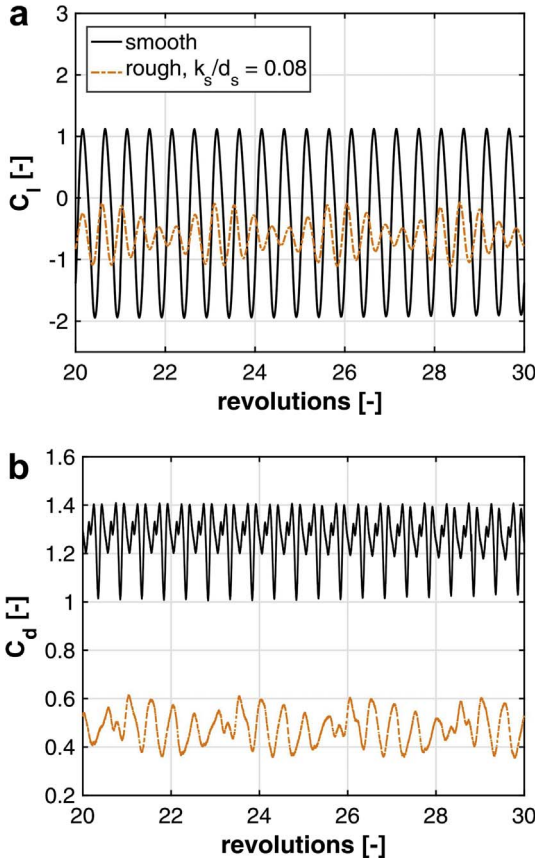

Fig. 13. Instantaneous (a) lift and (b) drag coefficients for the last 10 turbine revolutions.

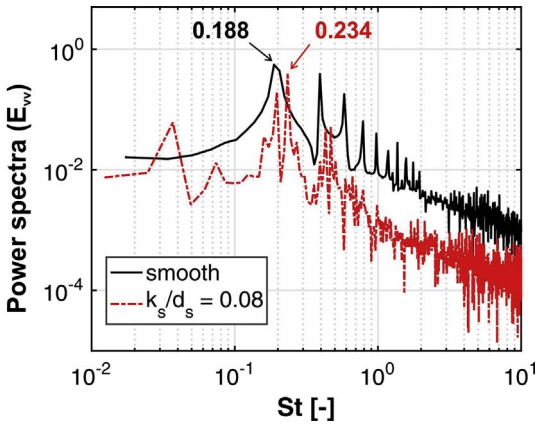

Fig. 14. Power spectra of the lateral velocity component (E_{vv}) in the wake of the shaft at $x/d_s = 1$ and $y/d_s = 0.5$.

instantaneous C_l and C_d shown in Fig. 13.

A comparison of time-averaged (over the last turbine revolution) distributions of pressure coefficient (*CoP*) over the smooth and rough shafts ($k_s/d_s = 0.08$) is given in Fig. 17a. It is shown that the pressure difference between fore ($0^\circ \leq \varphi < 90^\circ$ and $270^\circ < \varphi \leq 360^\circ$) and aft ($90^\circ \leq \varphi \leq 270^\circ$) halves of the shaft reduces significantly for the rough shaft, which is consistent with the substantial reduction in C_d observed in Fig. 13b. The asymmetry in the pressure distribution of both cases is a result of the counter-clockwise rotation of the shaft. The upper shaft surface moves against the freestream direction, leading to a lower relative velocity and a higher pressure at $\varphi \approx 90^\circ$. The reverse occurs on the lower surface.

Skin friction coefficients C_f for the smooth and rough shaft ($k_s/d_s = 0.08$) are compared in Fig. 17b. Note that zero-crossings in this

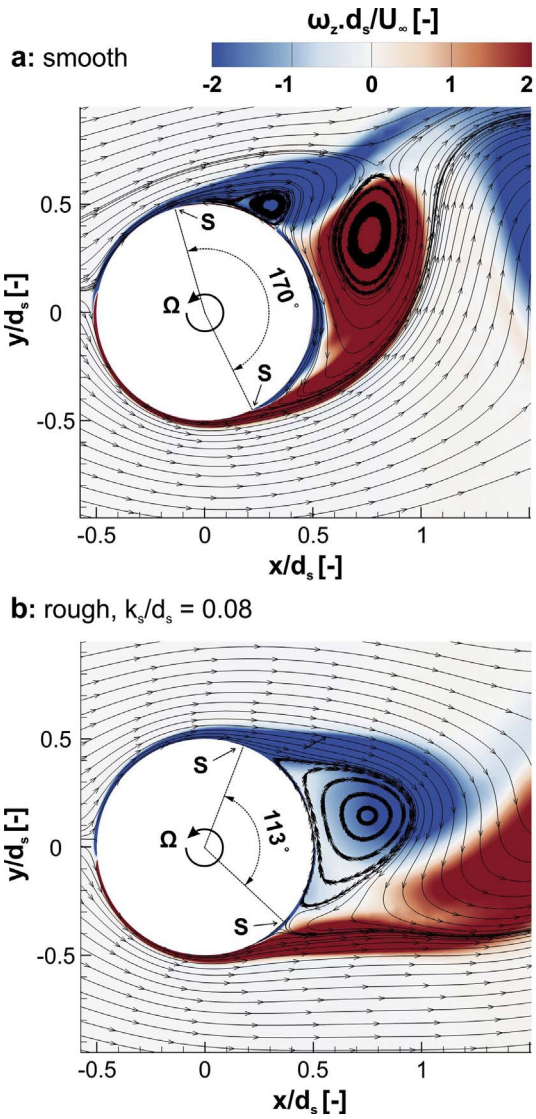

Fig. 15. Instantaneous contours of dimensionless out-of-plane vorticity (at the last time step with blades in most upwind and downwind positions) with superimposed streamlines near the rotating shaft. '*S*' denotes the separation points obtained from time-averaged observations.

Table 7
Separation point locations regarding the circumferential angle φ (see Fig. 1a) for the smooth and rough shafts, $k_s/d_s = 0.08$.

Surface	Smooth	Rough
Upper	74°	110°
Lower	244°	223°

plot can be used to detect flow separation. The comparison further confirms the delay in separation for the rough shaft on both upper and lower surfaces. For example, on the upper surface, the zero-crossing for the smooth shaft happens well before $\varphi = 90^\circ$ while this occurs beyond $\varphi = 90^\circ$ for the rough shaft.

The time-averaged (over 10 turbine revolutions) normalized streamwise velocity along the symmetry line $y/d = 0$, downstream of the shaft for $0.5 < x/d_s \leq 12.5$ ($0.02 < x/d \leq 0.5$) for the smooth and rough ($k_s/d_s = 0.08$) shafts is shown in Fig. 18. The higher mean velocity at the location where blades pass ($x/d = 0.5$) is apparent for the rough shaft. This is also the case for other lateral positions (not shown in this figure). The time-averaged (over 10 turbine revolutions)

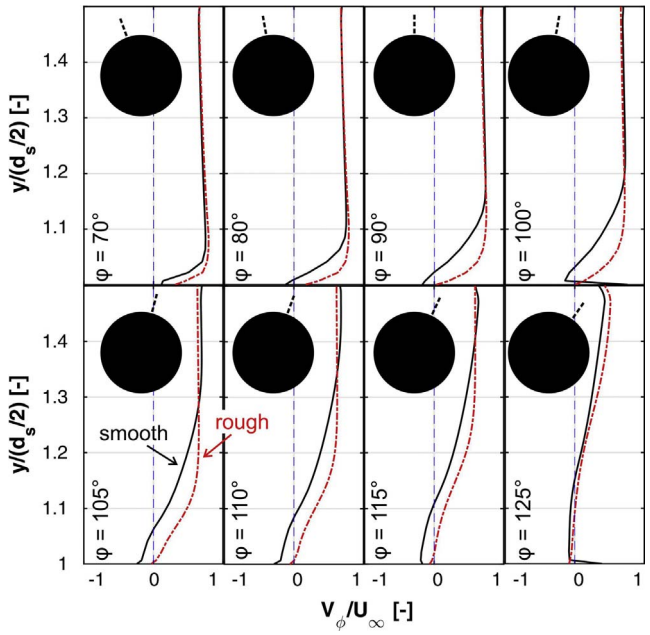

Fig. 16. Time-averaged (over 10 turbine revolutions) normalized tangential velocity profiles in the boundary layer for the smooth and rough shafts, $k_s/d_s = 0.08$. The black dashed lines perpendicular to the shaft schematic in the inset indicate the locations where data are plotted.

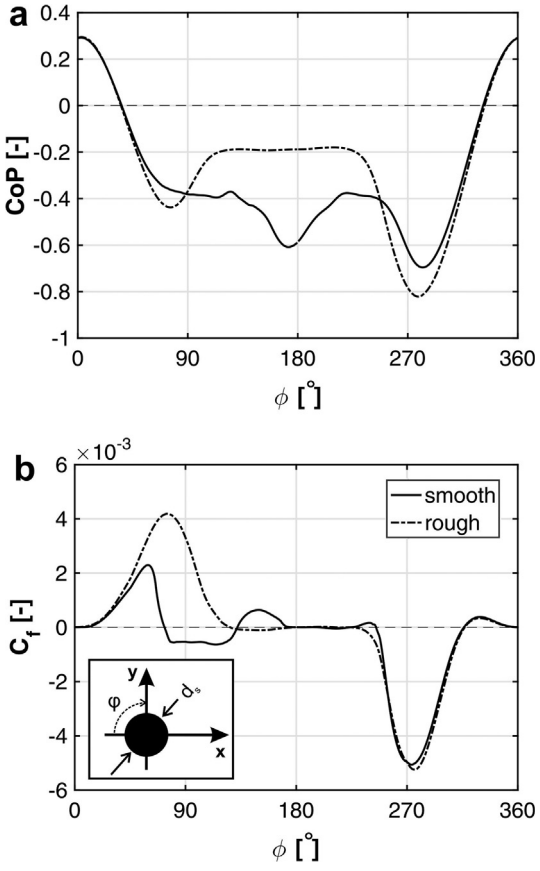

Fig. 17. Time-averaged (over 10 turbine revolutions) (a) pressure coefficient and (b) skin friction coefficient for the smooth and rough ($k_s/d_s = 0.08$) shafts.

normalized streamwise velocity along the lateral line $-2 \le y/d_s \le 2$ in different downstream locations $0.5 \le x/d_s \le 12.5$ ($0.02 \le x/d \le 0.5$) for the smooth and rough shafts is shown in Fig. 19. The smaller amount of separation and narrower shaft wake for the rough shaft can

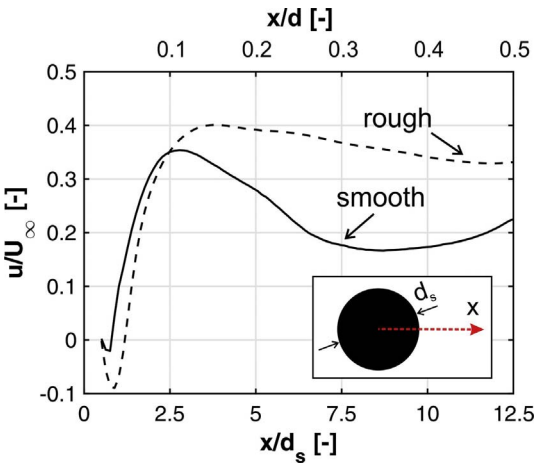

Fig. 18. Time-averaged (over 10 turbine revolutions) normalized streamwise velocity along the symmetry line $y/d = 0$, downstream of the smooth and rough ($k_s/d_s = 0.08$) shafts.

be observed. The recovery in the instantaneous moment coefficient of the turbine observed in Fig. 12 and the improvement in turbine C_P shown in Fig. 11a for the rough shaft are a direct result of these observations. In addition, the reduction in the shaft wake width results in a smaller length scale of vortical structures in the wake of the shaft with a higher vortex shedding frequency f. This explains the observed increase in St for the rough shaft shown in Fig. 14.

4.2. Impact of shaft-to-turbine rotational speed ratio

The impact of the shaft-to-turbine rotational speed ratio η, given by Eq. (3), on the performance of the turbine for a rough shaft with the optimal roughness height identified in Section 4.1 ($k_s/d_s = 0.08$) is studied for η ranging from 0 to 1. This is important as it can determine to which extent results obtained in Section 4.1 (for $\eta = 1$) depend on η. Note that the value of $\eta = 0$ corresponds to a stationary shaft while $\eta = 1$ means that the shaft is rotating at the same speed and direction as the turbine. Fig. 20 shows a negligible difference on C_m and C_P ($< 0.2\%$) within the studied range. Therefore, the identified aerodynamic performance of the turbine in Section 4.1 is not significantly affected by η.

5. Conclusions

URANS calculations are performed to study the effect of the shaft on the aerodynamic performance of urban-scale VAWTs. Turbulence is modeled using the 3-equation k-ω SST model with the intermittency transition submodel. The evaluations are based on two sets of validation studies for VAWTs. Furthermore, as the focus of the paper is on the effect of the shaft on turbine performance, separate validation studies are performed for flow over smooth and rough cylinders. Investigated parameters are the shaft-to-turbine diameter ratio δ, the dimensionless shaft surface roughness k_s/d_s and the shaft-to-turbine rotational speed ratio η. In addition, the impact of several operational and geometrical parameters on the turbine power loss due to the presence of the shaft is investigated. The following conclusions can be drawn:

- The power loss of the turbine regarding reduction in C_P increases asymptotically from 0 to 5.5%for δ from 0 to 16%. This is due to the larger low-velocity wake region behind the shaft, where the blades pass through on the downwind side of the turbine. For large values of δ ($> 4\%$), the interaction between the vortices shed from the shaft, and the blades significantly increases.
- Increasing chord-based Reynolds number, inlet turbulence intensity, solidity and number of blades are found to decrease the turbine

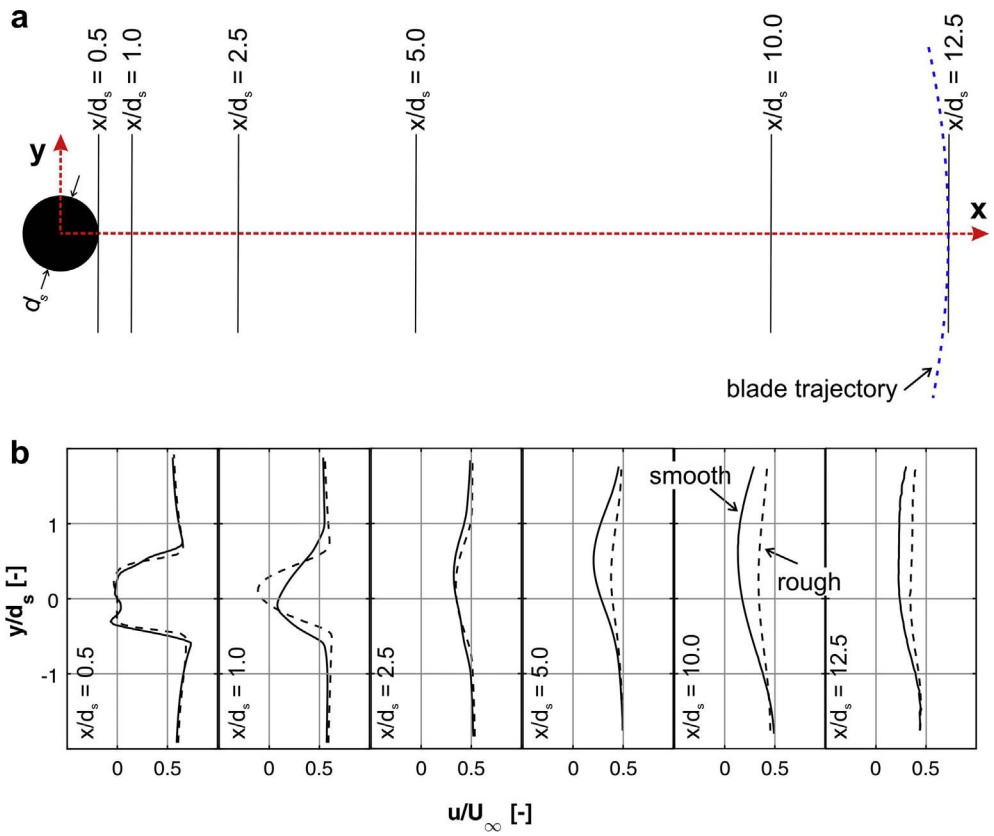

Fig. 19. (a) Downstream lateral sampling lines in the wake of the turbine shaft; (b) time-averaged (over 10 turbine revolutions) normalized streamwise velocity along these lines for the smooth and rough (k_s/d_s = 0.08) shafts.

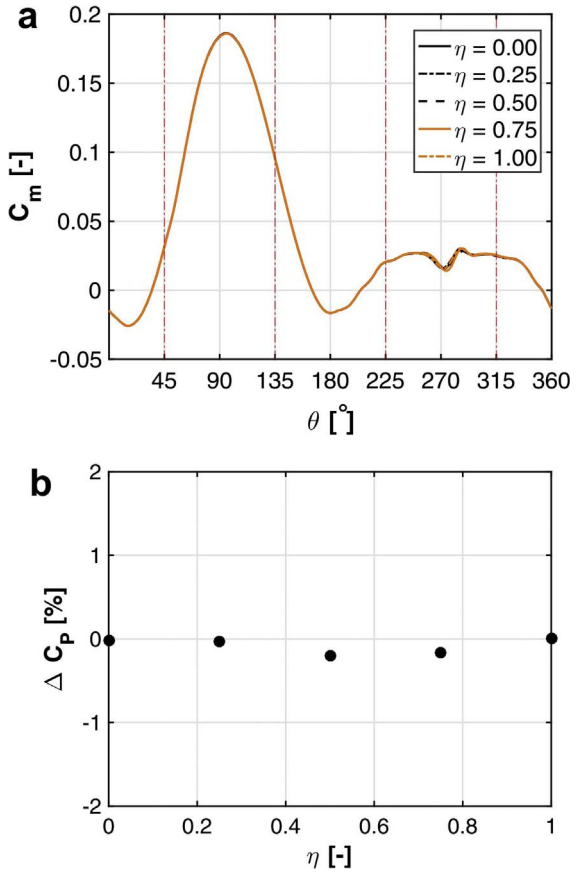

Fig. 20. (a) Instantaneous moment coefficient and (b) relative change of C_P concerning η = 1 for the last turbine revolution with different η.

power loss due to the presence of the shaft $|\Delta C_P|$. The minimum $|\Delta C_P|$ occurs at the optimum tip speed ratio, where C_P is maximum.
- The rotating shaft for an urban-scale VAWT operates in the subcritical regime with a Re_s which is one order of magnitude lower than that of the blade. This results in a high drag coefficient C_d for the shaft.

The addition of surface roughness is systematically investigated. The following conclusions are made:

- The flow over the shaft is shifted from subcritical to critical. Several parameters are employed to establish that this change in flow regime occurs between the smooth shaft and the rough shaft (with optimal roughness height k_s/d_s = 0.08):
  a. A delay in separation point over both the upper (from φ = 74° to 110°) and lower (from φ = 223° to 244°) surfaces of the turbine shaft and a consequent notable reduction in the shaft wake width;
  b. A jump in Strouhal number from 0.19 to 0.23;
  c. A significant reduction in average shaft drag.
- Because of the shift from subcritical to critical, the separation on the shaft is delayed and, as a result, the shaft wake width decreases and a larger mean velocity is present at the downstream turbine blades' trajectory. This means that the blades pass through a smaller wake region with higher mean velocity and consequently turbine performance is improved.
- An optimal shaft surface equivalent sand-grain roughness height of k_s/d_s = 0.08 is found to improve the turbine C_P by over 1.7%, leading to a 69% recovery of the power loss due to the presence of the shaft (δ = 4%).
- Within the range of parameters studied, the impact of the shaft-to-turbine rotational speed ratio (η) on the performance of the turbine is negligible.

It should be noted that the focus of the current study is to quantify

the turbine power loss associated with the shaft for an urban-scale VAWT and to show that employment of an optimal roughness height can significantly recover the identified power loss and improve turbine performance. From a practical point of view, adding roughness to the shaft is a simple and inexpensive method. Therefore, investigation of the performance of the turbine with a rough shaft at other tip speed ratios, solidities and blade shapes can be very intriguing for future research. Furthermore, three-dimensional CFD calculations and the application of more advanced hybrid RANS-LES methods can provide further details of the 3D and unsteady nature of the interactions between the vortices shed by the shaft and the blades passing downstream.

Acknowledgements

The authors would like to acknowledge support from the European Commission's Framework Program Horizon 2020, through the Marie Curie Innovative Training Network (ITN) AEOLUS4FUTURE - Efficient harvesting of the wind energy (H2020-MSCA-ITN-2014: Grant agreement no. 643167) and the TU1304 COST ACTION “WINERCOST”. The authors gratefully acknowledge the partnership with ANSYS CFD. This work was sponsored by NWO Exacte Wetenschappen (Physical Sciences) for the use of supercomputer facilities, with financial support from the Nederlandse Organisatie voor Wetenschappelijk Onderzoek (Netherlands Organization for Scientific Research, NWO). The 3rd author, Hamid Montazeri, is currently a postdoctoral fellow of the Research Foundation – Flanders (FWO) and is grateful for its financial support (project FWO 12M5316N).

References

[1] Bedon G, Schmidt Paulsen U, Aagaard Madsen H, Belloni F, Raciti Castelli M, Benini E. Computational assessment of the DeepWind aerodynamic performance with different blade and airfoil configurations. Appl Energy 2017;185(2):1100–8.
[2] Cheng Z, Madsen HA, Gao Z, Moan T. A fully coupled method for numerical modeling and dynamic analysis of floating vertical axis wind turbines. Renew Energy 2017;107:604–19.
[3] Cheng Z, Madsen HA, Gao Z, Moan T. Effect of the number of blades on the dynamics of floating straight-bladed vertical axis wind turbines. Renew Energy 2017;101:1285–98.
[4] Tummala A, Velamati RK, Sinha DK, Indraja V, Krishna VH. A review on small scale wind turbines. Renew Sustain Energy Rev 2016;56:1351–71.
[5] Müller G, Chavushoglu M, Kerri M, Tsuzaki T. A resistance type vertical axis wind turbine for building integration. Renew Energy 2017;111:803–14.
[6] Gsänger S, Pitteloud JD. Small wind world report summary. World Wind Energy Association (WWEA); 2015.
[7] Bianchini A, Balduzzi F, Ferrara G, Ferrari L. A computational procedure to define the incidence angle on airfoils rotating around an axis orthogonal to flow direction. Energy Convers Manage 2016;126:790–8.
[8] Bianchini A, Balduzzi F, Ferrara G, Ferrari L. Virtual incidence effect on rotating airfoils in Darrieus wind turbines. Energy Convers Manage 2016;111:329–38.
[9] Tsai H-C, Colonius T. Coriolis effect on dynamic stall in a vertical axis wind turbine. AIAA Journal 2016;54(1):216–26.
[10] Simão Ferreira C, van Kuik G, van Bussel G, Scarano F. Visualization by PIV of dynamic stall on a vertical axis wind turbine. Exp Fluids 2008;46(1):97–108.
[11] Bianchini A, Balduzzi F, Bachant P, Ferrara G, Ferrari L. Effectiveness of two-dimensional CFD simulations for Darrieus VAWTs: a combined numerical and experimental assessment. Energy Convers Manage 2017;136:318–28.
[12] Abkar M, Dabiri JO. Self-similarity and flow characteristics of vertical-axis wind turbine wakes: an LES study. J Turbul 2017;18(4):373–89.
[13] Ryan KJ, Coletti F, Elkins CJ, Dabiri JO, Eaton JK. Three-dimensional flow field around and downstream of a subscale model rotating vertical axis wind turbine. Exp Fluids 2016;57(3).
[14] Araya DB, Colonius T, Dabiri JO. Transition to bluff-body dynamics in the wake of vertical-axis wind turbines. J Fluid Mech 2017;813:346–81.
[15] Yu JM, Leu TS, Miau JJ. Investigation of reduced frequency and freestream turbulence effects on dynamic stall of a pitching airfoil. J Visual 2017;20(1):31–44.
[16] Li Q, Maeda T, Kamada Y, Murata J, Shimizu K, Ogasawara T, et al. Effect of solidity on aerodynamic forces around straight-bladed vertical axis wind turbine by wind tunnel experiments (depending on number of blades). Renew Energy 2016;96:928–39.
[17] Simão Ferreira C, Geurts B. Aerofoil optimization for vertical-axis wind turbines. Wind Energy 2014;18(8):1371–85.
[18] Roh S-C, Kang S-H. Effects of a blade profile, the Reynolds number, and the solidity on the performance of a straight bladed vertical axis wind turbine. J Mech Sci Technol 2013;27(11):3299–307.
[19] Shen X, Yang H, Chen J, Zhu X, Du Z. Aerodynamic shape optimization of non-straight small wind turbine blades. Energy Convers Manage 2016;119:266–78.
[20] Subramanian A, Yogesh SA, Sivanandan H, Giri A, Vasudevan M, Mugundhan V, et al. Effect of airfoil and solidity on performance of small scale vertical axis wind turbine using three dimensional CFD model. Energy 2017;133:179–90.
[21] Eboibi O, Danao LAM, Howell RJ. Experimental investigation of the influence of solidity on the performance and flow field aerodynamics of vertical axis wind turbines at low Reynolds numbers. Renew Energy 2016;92:474–83.
[22] Fiedler AJ, Tullis S. Blade offset and pitch effects on a high solidity vertical axis wind turbine. Wind Eng 2009;33(3):237–46.
[23] Rezaeiha A, Kalkman I, Blocken B. Effect of pitch angle on power performance and aerodynamics of a vertical axis wind turbine. Appl Energy 2017;197:132–50.
[24] Shahizare B, Nik-Ghazali N, Chong WT, Tabatabaeikia S, Izadyar N, Esmaeilzadeh A. Novel investigation of the different Omni-direction-guide-vane angles effects on the urban vertical axis wind turbine output power via three-dimensional numerical simulation. Energy Convers Manage 2016;117:206–17.
[25] Scungio M, Arpino F, Focanti V, Profili M, Rotondi M. Wind tunnel testing of scaled models of a newly developed Darrieus-style vertical axis wind turbine with auxiliary straight blades. Energy Convers Manage 2016;130:60–70.
[26] Chong WT, Hew WP, Yip SY, Fazlizan A, Poh SC, Tan CJ, et al. The experimental study on the wind turbine’s guide-vanes and diffuser of an exhaust air energy recovery system integrated with the cooling tower. Energy Convers Manage 2014;87:145–55.
[27] Morgulis N, Seifert A. Fluidic flow control applied for improved performance of Darrieus wind turbines. Wind Energy 2015;19(9):1585–602.
[28] Greenblatt D, Lautman R. Inboard/outboard plasma actuation on a vertical-axis wind turbine. Renew Energy 2015;83:1147–56.
[29] Yen J, Ahmed NA. Enhancing vertical axis wind turbine by dynamic stall control using synthetic jets. J Wind Eng Ind Aerodyn 2013;114:12–7.
[30] Wang Y, Sun X, Dong X, Zhu B, Huang D, Zheng Z. Numerical investigation on aerodynamic performance of a novel vertical axis wind turbine with adaptive blades. Energy Convers Manage 2016;108:275–86.
[31] Sobhani E, Ghaffari M, Maghrebi MJ. Numerical investigation of dimple effects on darrieus vertical axis wind turbine. Energy 2017;133:231–41.
[32] Cai X, Gu R, Pan P, Zhu J. Unsteady aerodynamics simulation of a full-scale horizontal axis wind turbine using CFD methodology. Energy Convers Manage 2016;112:146–56.
[33] Snel H. Review of aerodynamics for wind turbines. Wind Energy 2003;6(3):203–11.
[34] Hansen MOL, Aagaard Madsen H. Review paper on wind turbine aerodynamics. J Fluids Eng 2011;133(11):114001.
[35] Santoni C, Carrasquillo K, Arenas-Navarro I, Leonardi S. Effect of tower and nacelle on the flow past a wind turbine. Wind Energy 2017. http://dx.doi.org/10.1002/we.2130.
[36] Rezaeiha A, Pereira R, Kotsonis M. Fluctuations of angle of attack and lift coefficient and the resultant fatigue loads for a large horizontal axis wind turbine. Renew Energy 2017;114(Part B):904–16. http://dx.doi.org/10.1016/j.renene.2017.07.101.
[37] Norberg C, Sunden B. Turbulence and Reynolds number effects on the flow and fluid forces on a single cylinder in cross flow. J Fluids Struct 1984;1(3):337–57.
[38] Batham JP. Pressure distributions on circular cylinders at critical Reynolds numbers. J Fluid Mech 1973;57(2):209–28.
[39] Achenbach E. Distribution of local pressure and skin friction around a circular cylinder in cross-flow up to $Re = 5 \times 10^6$. J Fluid Mech 1968;34(4):625–39.
[40] Achenbach E. Influence of surface roughness on the cross-flow around a circular cylinder. J Fluid Mech 1971;48(2):321–35.
[41] Achenbach E, Heinecke E. On vortex shedding from smooth and rough cylinders in the range of Reynolds numbers 6×10^3 to 5×10^6. J Fluid Mech 1981;109:239–51.
[42] Guven O, Farell C, Patel VC. Surface-roughness effects on the mean flow past circular cylinders. J Fluid Mech 1980;98(4):673–701.
[43] Nakamura Y, Tomonari Y. The effects of surface roughness on the flow past circular cylinders at high Reynolds numbers. J Fluid Mech 1982;123:363–78.
[44] Ingham DB. Steady flow past a rotating cylinder. Comput Fluids 1983;11(4):351–66.
[45] Badr HM, Coutanceau M, Dennis SCR, Menard C. Unsteady flow past a rotating circular cylinder at Reynolds numbers 10^3 and 10^4. J Fluid Mech 1990;220:459–84.
[46] Tokumaru PT, Dimotakis PE. The lift of a cylinder executing rotary motions in a uniform flow. J Fluid Mech 1993;225:1–10.
[47] Mittal S, Kumar B. Flow past a rotating cylinder. J Fluid Mech 2003;476:303–34.
[48] Cantwell B, Coles D. An experimental study of entrainment and transport in the turbulent near wake of a circular cylinder. J Fluid Mech 2006;136:321–74.
[49] Castelli MR, Englaro A, Benini E. The Darrieus wind turbine: proposal for a new performance prediction model based on CFD. Energy 2011;36(8):4919–34.
[50] Tescione G, Ragni D, He C, Simão Ferreira C, van Bussel GJW. Near wake flow analysis of a vertical axis wind turbine by stereoscopic particle image velocimetry. Renew Energy 2014;70:47–61.
[51] Rezaeiha A, Kalkman I, Blocken B. CFD simulation of a vertical axis wind turbine operating at a moderate tip speed ratio: guidelines for minimum domain size and azimuthal increment. Renew Energy 2017;107:373–85.
[52] Buresti G. The effect of surface roughness on the flow regime around circular cylinders. J Wind Eng Ind Aerodyn 1981;8:105–14.
[53] Fage A, Warsap JH. The effects of turbulence and surface roughness on the drag of a circular cylinder. Reports and memoranda no. 1283; 1930.
[54] Blocken B, Stathopoulos T, Carmeliet J. CFD simulation of the atmospheric boundary layer: wall function problems. Atmos Environ 2007;41(2):238–52.
[55] Blocken B, Carmeliet J, Stathopoulos T. CFD evaluation of wind speed conditions in

passages between parallel buildings—effect of wall-function roughness modifications for the atmospheric boundary layer flow. J Wind Eng Ind Aerodyn 2007;95(9–11):941–62.
[56] ANSYS, ANSYS® fluent theory guide, release 16.1, ANSYS Inc; 2015.
[57] Palkin E, Mullyadzhanov R, Hadžiabdić M, Hanjalić K. Scrutinizing URANS in shedding flows: the case of cylinder in cross-flow in the subcritical regime. Flow Turbul Combust 2016;97(4):1017–46.
[58] Menter FR, Langtry RB, Likki SR, Suzen YB, Huang PG, Völker S. A correlation-based transition model using local variables—part I: model formulation. J Turbomach 2006;128(3):413–22.
[59] Langtry RB, Menter FR, Likki SR, Suzen YB, Huang PG, Völker S. A correlation-based transition model using local variables—part II: test cases and industrial applications. J Turbomach 2006;128(3):423–34.
[60] Zheng Z, Lei J. Application of the γ-Re θ transition model to simulations of the flow past a circular cylinder. Flow Turbul Combust 2016;97(2):401–26.
[61] Cebeci T, Bradshaw P. Momentum transfer in boundary layers. New York: Hemisphere Publishing Corporation; 1977.
[62] Nikuradse L. Laws of flow in rough pipes, VDI Forsch. 361. English translation. NACA TM-1292 (1965); 1933.
[63] Schlichting H, Boundary-layer theory, 8th rev. ed. New York: Springer; 2000.
[64] Tutar M, Holdø AE. Computational modelling of flow around a circular cylinder in sub-critical flow regime with various turbulence models. Int J Numer Meth Fluids 2001;35:763–84.
[65] Rodi W. Comparison of LES and RANS calculations of the flow around bluff bodies. J Wind Eng Ind Aerodyn 1997;69–71:55–75.
[66] Lübcke H, Schmidt S, Rung T, Thiele F. Comparison of LES and RANS in bluff-body flow. J Wind Eng Ind Aerodyn 2001;89:1471–85.
[67] Hanjalic K. Will RANS survive LES? A view of perspectives. J Fluids Eng 2005;127(5):831.
[68] Roache PJ. Quantification of uncertainty in computational fluid dynamics. Annu Rev Fluid Mech 1997;29:123–60.
[69] Rezaeiha A, Montazeri H, Blocken B. Towards accurate CFD simulations of vertical axis wind turbines at different tip speed ratios and solidities: guidelines for convergence, azimuthal increment and domain size; 2017 [submitted for publication].
[70] Gad-el-Hak M, Bushnell DM. Separation control: review. J Fluids Eng 1991;113(1):5–30.